Corrosion-resistant composite coatings based on a graphene oxide–metal oxide/urushiol formaldehyde polymer system

Lei Zhang, Wupin Wang, Haitang Wu, Zeyu Zheng, Ming Wei, Xiaohua Huang

Abstract Composite coatings were fabricated based on a graphene oxide–metal oxide/urushiol formaldehyde polymer (GO–TiO$_2$/UFP, GO–SiO$_2$/UFP and GO–Y$_2$O$_3$/UFP) system with modifications, and its effectiveness in corrosion protection of metal substrates was demonstrated. First, a GO–TiO$_2$ composite was synthesized using titanium dioxide loading on GO via 3-aminopropyltriethoxysilane (APTES). The GO–Y$_2$O$_3$ composite was synthesized using nano-yttrium oxide intercalating into GO through two different silane coupling agents. The GO–SiO$_2$ composite was synthesized via an in-situ two-step sol-gel process utilizing APTES and tetraethylorthosilicate (TEOS) in an aqueous ethanol solution. The morphology and structure of the GO–metal oxide composites (GO–TiO$_2$, GO–Y$_2$O$_3$ and GO–SiO$_2$) were studied. Subsequently, GO–metal oxides were incorporated into UFP to investigate the composite's effectiveness in corrosion protection of metal substrates. Compared with GO–TiO$_2$/UFP and GO–Y$_2$O$_3$/UFP, GO–SiO$_2$/UFP showed superior alkali-resistance enhancing performance. Additionally, GO crosslinked with APTES–TiO$_2$ via covalent bonds and the well-dispersed GO–TiO$_2$ in UFP improved the electrochemical corrosion properties of the UFP coatings, most likely due to the obstruction of the diffusion pathways inside the UFP coating matrix, thus preventing the diffusion of penetrating species. It was revealed that the corrosion resistance of GO–TiO$_2$/UFP composite coating was noticeably higher than GO–SiO$_2$/UFP and GO–Y$_2$O$_3$/UFP composite coatings.

Keywords Urushiol-formaldehyde polymer, Graphene oxide, Silica, Titanium dioxide, Yttrium oxide, Alkali resistance

L. Zhang, H. Wu (✉), X. Huang (✉)
Key Laboratory of Exploitation and Utilization of Economic Plant Resources of Shaanxi Province, College of Forestry, Northwest A&F University, 3 Taicheng Road, Yangling 712100, China
e-mail: haitangwu@hotmail.com

X. Huang
e-mail: 1067716566@qq.com

L. Zhang
Research Institute of Chemical Defense, Academy of Military Sciences, Changping District, Beijing 102205, People's Republic of China

W. Wang
Xi'an Research Institute of Chinese Lacquer Under All China Federation of Supply and Marketing Cooperatives, Xixian New District, Xi'an 712000, China

Z. Zheng, M. Wei
Wuhan University of Technology, 122 Luo Shi Road, Wuhan 430070, China

Introduction

Urushiol formaldehyde polymers (UFPs) are usually used in corrosion protection.[1] However, their low alkali resistance greatly limits their application scope, and it is thus necessary to enhance the alkali resistance of UFP.[2] Incorporation of dispersed graphene oxide (GO)–nano oxide can efficiently obstruct micropores by reducing internal stresses, thus enhancing the barrier properties of UFP-containing film as a nano-filler.[3–5]

GO has been successfully used to improve the formulation and anticorrosive properties of polymer coatings.[1,2,6] The development of composite coatings functionalized by GO-polymers could effectively enhance the anticorrosion and physico-mechanical properties of anticorrosive coatings used for industrial equipment.[7] Currently, GO is mainly fabricated from natural graphite via the modified Hummers method,[8,9]

which produces a nonuniform distribution of oxygen functional groups (carboxylic at the edges, hydroxyl on the surface and epoxide in the basal plane) on the graphene sheets. The preparation of GO-polymer composite coatings for various fields is strongly limited by the low dispersibility of GO. However, a variety of processing methods for improved dispersion of GO in polymer composites have been recently developed, including surface grafting and decorating with nanoparticles, in situ polymerization and organic modification.[8,10,11] In particular, some studies have reported that the properties of GO can be improved by decorating it with nanoparticles such as oxides of titanium, aluminum, yttrium and zinc, as well as silica.[12–17] At the same time, organic coatings comprising blended GO decorated with nanoparticles were introduced to achieve better dispersion of GO by preventing it from aggregating within the polymer coating.[12]

Nano-TiO$_2$ has been widely applied as a polymer filler in organic coatings because of its high resistance to weathering and corrosion. Nevertheless, the high polarity and large surface area of nano-TiO$_2$ particles make them prone to aggregation in polymer coatings.[13,18,19] In addition, nano-silica (SiO$_2$) was introduced into polymeric composite coatings which showed high corrosion resistance and mechanical properties. These were characterized by nano-SiO$_2$ chain-like aggregates characterized by hydrogen bonds between the polymer and the surface hydroxyls of the nanoparticles.[20–24] Similarly, nano-yttrium oxide has been exploited as a very promising additive to polymeric organic coatings on metal substrates, owing to its high thermal and chemical stability,[25,26] as well as good mechanical and barrier properties.[27,28] An as–fabricated GO–oxide dispersed composite was added into a polymeric organic coating, which not only greatly improved the corrosion resistance of the polymer coating but also improved the dispersion of nanoparticles within the matrix via a loose structure of GO.[29]

With potentially important applications and theoretical implications, the GO–metal oxide composites were prepared via a novel route in this study, which not only combined their inherent advantages but also improved the dispersion of GO within UFP. The synthesis of GO–TiO$_2$ was conducted using 3-aminopropyltriethoxysilane (APTES), GO–SiO$_2$ was fabricated via a sol-gel method using APTES and TEOS, while GO–Y$_2$O$_3$ was prepared via a chemical reaction between GPS–Y$_2$O$_3$ and APS–GO. Afterward, the GO–TiO$_2$, GO–SiO$_2$ and GO–Y$_2$O$_3$ particles were dispersed in UFP as nanofillers, and the corresponding UFP composite coatings were obtained via a solution-blending process. Finally, differences in the resistance of the resulting composite coatings against corrosion and alkali were investigated.

Materials and methods

Materials

Graphite powder with < 20 μm particle size was sourced from the Chinese Academy of Sciences Chengdu Organic Chemical Co., Ltd. (China). Nano-TiO$_2$ (about 30 nm) was supplied by Guangzhou Metal Metallurgy Co., Ltd. (China). Nano-Y$_2$O$_3$ (about 20 nm) was purchased from Ji'nan Huasen Metal Products Co., Ltd. (China). Tetraethyl orthosilicate (TEOS) was sourced from Tianjin Kermel Chemical Reagent Co., Ltd. (China), and the silane coupling agents (SCA): (3-amino-propyl)-trimethoxysilane (APS), γ-(2,3-epoxypropoxy)propyl-trimethoxy silane (GPTMS) and 3-aminopropyltriethoxysilane (APTES) were obtained from Nanjin Chuanshi Chem Co., Ltd. (China). Pure urushiol was obtained via xylene extraction of raw lacquer sap (Shaanxi Lacquer Culture Industry Co., Ltd. China), as described previously.[30] Analytical-grade potassium permanganate, hydrogen peroxide, aqueous ammonia solution, hydrochloric acid, sulfuric acid, xylene, methanol, formaldehyde, ethanol and acetone were commercially available.

Fabrication process of the composite coatings

Synthesis of APTES-GO

The modified Hummers method was used to synthesize graphene oxide (GO) from natural graphite.[31] Briefly, 1 g of APTES and 0.05 g of GO were first suspended in 50 g of anhydrous ethanol ultrasonication at 50°C for 60 min. Subsequently, the resulting solution was stirred in a water bath at 80°C for 4 h. Then, 5 g distilled water was dropped into the mixed solution, and the as-prepared solution filtrated and washed several times with a 50% (v/v) aqueous ethanol solution to remove the unreacted coupling agents. The obtained solid was dried for 24 h at 60°C to obtain APTES-GO powder. The synthesis of APS–GO powder using the second silane coupling agent APS was done in analogy to that of APTES-GO.

Synthesis of GO–SiO$_2$

A one-step sol-gel process was used to prepare the nano-GO–SiO$_2$.[32,33] A schematic of the GO–SiO$_2$ fabrication process is shown in Fig. 1. Specifically, 0.05 g of APTES-GO was added to 288 mL of an aqueous ethanol solution (240 mL ethanol and 40 mL DI water) and dispersed by ultrasonication at 50°C for 60 min to form a homogenous solution. Subsequently, 360 μL of a 28% (w/v) aqueous ammonia solution and 0.6 mL of TEOS were dissolved in the APTES-GO suspension in a 500-mL three-necked condenser flask with a magnetic stirrer. The reaction was performed at
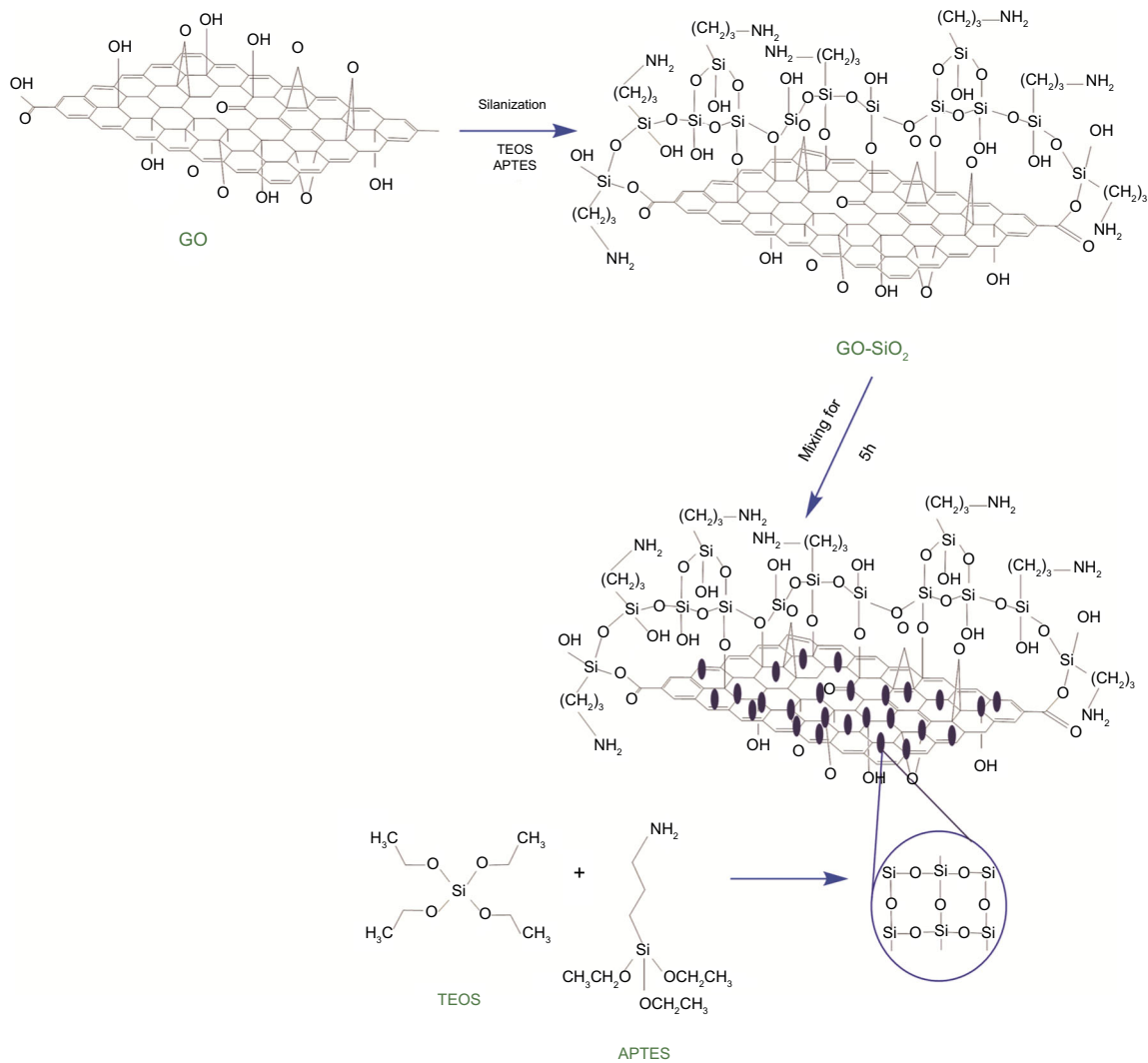
Fig. 1: A schematic illustration of the GO–SiO$_2$ synthesis procedure

60°C in a water bath for 4 h to ensure the complete hydrolysis of the mixture, followed by incubation of 75°C for another 1 h. The as-prepared solution was filtrated and washed several times with a 50% (v/v) aqueous ethanol solution to remove the unreacted coupling agents, and the solid was dried for 24 h at 60°C to obtain GO–SiO$_2$ powder.

Synthesis of GO–TiO$_2$

As illustrated in Fig. 2, the preparation of GO–TiO$_2$ followed a two-step method as follows:

(1) 6 g of APTES and 0.2 g of nano–TiO$_2$ were suspended in 150 g of anhydrous ethanol by ultrasonication at 50°C for 30 min. The resulting solution was stirred for 6 h in a water bath at 80°C, after which 44 g of a 15/7 (w/w) aqueous/ethanol solution were dropped into the mixed solution. Finally, the as-prepared solution was

filtrated and washed several times with the aqueous ethanol solution to remove the unreacted coupling agents. The remaining solid was dried for 24 h at 60°C to obtain APTES–TiO$_2$.

(2) 0.3 g of GO and 0.2 g of APTES–TiO$_2$ were added to 100 mL of xylene and uniformly dispersed through ultrasonication for 30 min. The reaction mixture was stirred for 3 h at 105°C, and the resulting GO–TiO$_2$ was obtained by filtrating, washing five times with anhydrous ethanol, and drying for 24 h at 60°C, followed by repeated grinding to obtain a powder.

Synthesis of GPS–Y$_2$O$_3$ and GO–Y$_2$O$_3$

The amino-functionalized Y$_2$O$_3$ was obtained using GPS to modify nano-Y$_2$O$_3$. Briefly, 0.1 g of nano–Y$_2$O$_3$ and 2 g of GPS were homogeneously dispersed in 100 g of anhydrous ethanol by ultrasonication at 50°C for 30
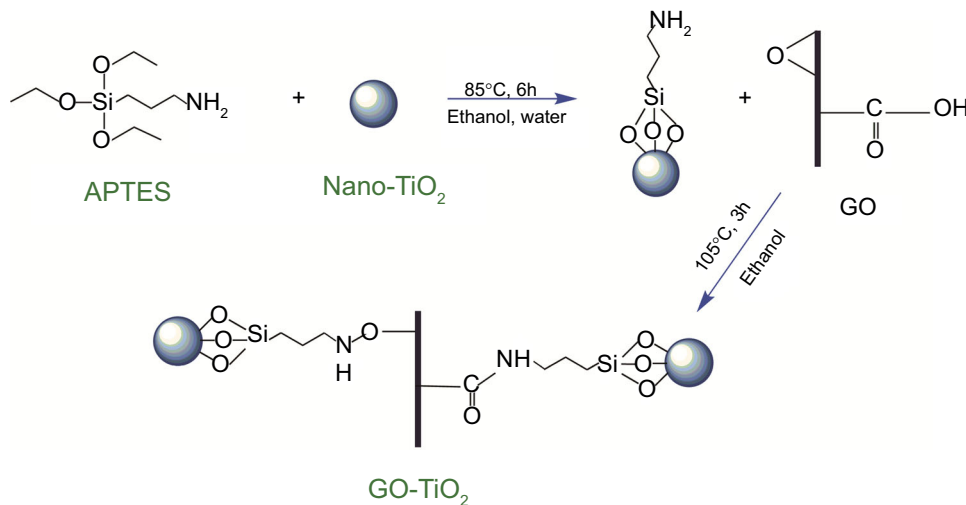
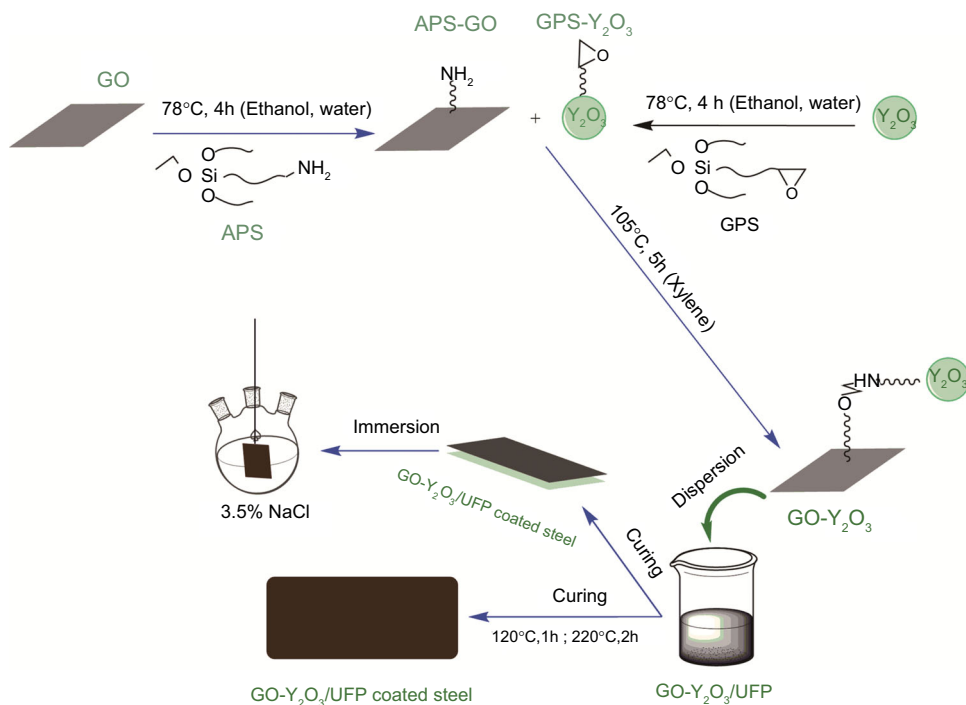**Fig. 2: A schematic illustration of the GO–TiO$_2$ synthesis procedure**

Fig. 3: A schematic illustration of the preparation of GO–Y$_2$O$_3$ and the corresponding UFP coatings

min. The resulting solution was stirred for 4 h in a water bath at 78°C with drop-wise addition of DI water (10 g). Finally, the as-prepared solution was filtered and washed several times with a 50% (*v/v*) aqueous ethanol solution to remove the unreacted chemicals. The remaining solid was dried for 24 h at 60°C to obtain GPS–Y$_2$O$_3$.

A schematic representation of the reaction between APS–GO and GPS–Y$_2$O$_3$ is shown in Fig. 3. An aliquot comprising 0.25 g of APS–GO was added to 100 mL of xylene and dispersed through ultrasonication for 30 min. Subsequently, 0.05 g of GPS–Y$_2$O$_3$ was added

into the suspension and dispersed via ultrasonication for 30 min. The resulting mixed solution was stirred for 5 h at 105°C, after which the GO–Y$_2$O$_3$ solid was filtered, washed several times with a 50% (*v/v*) aqueous ethanol to remove the unreacted coupling agents, and dried at 60°C for 24 h.

Preparation of the UFP composite coatings

A homogeneous distribution of nanofiller was ensured by using a low content of GO–TiO$_2$, GO–SiO$_2$ and

GO–Y_2O_3 in the organic coating to prevent them from agglomerating within the UFP matrix. For this purpose, the modified GO dispersion in xylene (1:30, *w/w*) was sonicated for 30 min and then added to a stoichiometric amount of UFP resin at room temperature using an S312-250H high shear mechanical mixer (SENCO Technology Co., Ltd., China). The mixing ratio of UFP to modified GO was 100:1 by weight. The prepared coatings were applied to JDMK-50 tinplates (Tianjin Jingkelian Material Testing Machine Co., Ltd., China) using the roll coating technique.[33] The UFP composite coated tinplates were sequentially baked at 120°C for 1 h and 220°C for 2 h in an oven to achieve complete curing. In addition, the 30 μm thickness GO-metal oxide/UFP composite coatings were prepared on the tinplates and glass sheets as a reference sample.

Characterization of composite coatings

The FTIR test was performed in a wavelength range of 400–4000 cm^{-1} using a NICOLET IS10 FTIR spectroscopy instrument (PerkinElmer, USA). A K-Alpha X-ray photoelectron spectrometer (XPS; Thermo Fisher Scientific, USA) was used as follows: Al Ka was used as the radiation source at 10^{-7} mbar and a voltage of 5 kV. An S-4800 field emission scanning electron microscope (FE-SEM, Hitachi Ltd., Japan) was used to examine the morphology of the prepared coatings. XRD (D8 ADVANCE A25, Bruker, Germany) was used to measure the phase crystallinity and composition of the prepared coatings, with Cu Ka as the radiation source at 40 kV and 30 mA.

A PGSTAT 30 electrochemical workstation was used for electrochemical impedance spectroscopy (EIS) and potentiodynamic polarization curve measurements, with a three-electrode cell configuration for both EIS tests and Tafel plots.[29] The measurement apparatus consisted of a 1 cm^2 tinplate sample coated with the modified GO–metal oxide/UFP as the working electrode, a platinum counter electrode and a saturated calomel electrode (SCE) as the reference electrode.[12,37] An applied potential range from − 0.25 to + 0.25 V and relative to open circuit potential (OCP) were used for the polarization curves test at a scan rate of 1 mV/s.[37] A frequency range from 0.01 Hz to 100 kHz, with a sinusoidal voltage of 10 mV, was used for the EIS test. All EIS measurements were implemented on three different replicates for checking the repeatability of data.

Analysis of chemical resistance properties

The anticorrosion properties of the UFP composite coatings were investigated using an induced corrosion experiment in chemical solutions. Individual coated glass sheets were separately immersed in 3% NaCl, 30% H_2SO_4 and 10% NaOH for 14 days at room temperature. Loss of color, brightness or the formation of foam on the surface of the coating were visually followed. Every 24 h, the samples were checked and photographed.

Results and discussion

FTIR analysis

A goal of the structural analysis was to investigate the completion of the reaction between GO and APTES–TiO_2. The FTIR spectra of GO–TiO_2/UFP and GO–TiO_2 are shown in Fig. 4a. The absorption peaks at 2920, 2843, 1038 and 1109 cm^{-1} could be attributed to the stretching vibrations of –CH_3 and –CH_2, as well as Si–O–C and Si–O–Si, respectively, most likely corresponding to the functional groups of APTES. The –NH_2 absorption band at 1640 cm^{-1} and the Ti–O–Ti stretching band at 765–620 cm^{-1} of GO–TiO_2 were observed. These results indicated that nano-TiO_2 had been successfully modified using silane molecules (APTES) through chemical reactions with functional groups.

When comparing typical spectra of GO–TiO_2 and GO, it can be seen that the stretching vibration of C–O–C (GO) at 1120 cm^{-1} disappeared along with appearance of the stronger –CN and –NH absorptions at 1545, 801 and 1545 cm^{-1}, respectively, which demonstrated the successful chemical reaction between epoxide groups on GO surface and amino groups from the modified nano–TiO_2 in APTES.[15]

The FTIR peaks of APS–GO, GPS–Y_2O_3, GO–Y_2O_3 and GO–Y_2O_3/UFP are shown in Fig. 4b. The distinctive absorption peaks of GO generally appear at 3447, 1220, 1120 and 1741 cm^{-1} corresponding to –OH, C–O, C–O–C and C=O, respectively, indicating the presence of hydroxyl, epoxide and carboxyl groups on the GO surface. Accordingly, the feature in the range of 2800–3000 cm^{-1} was the result of the –CH stretching modes in the FTIR spectra of APS–GO and GPS–Y_2O_3. The strong peaks at 1040 cm^{-1} were associated with Si–O–Si/Si–O–C bonding from APS and GPS,[34] with the appearance of new peaks at 1385 and 1508 cm^{-1} corresponding to Si–O–Y,[35] indicating the Y_2O_3 and GO have been successfully modified by the silane coupling agents APS and GPS through chemical bonding, accordingly. In the FTIR spectra of the GO–Y_2O_3 example, the absorption peaks of C–O–C bonding became obscured by the appearance of a stronger absorption at 1525 and 1410 cm^{-1} attributed to the bending of the secondary amide N–H and the C–N stretching vibration, while Si–O–Si/Si–O–C and Si–O–Y bonding was still observed (Fig. 4b). These results implied that reactions took place between the epoxide and amino groups to some extent.[36]

Figure 4c shows the FTIR spectra of APTES–GO and GO–SiO_2. In the spectrum of APTES–GO, many new characteristic absorption peaks were clearly

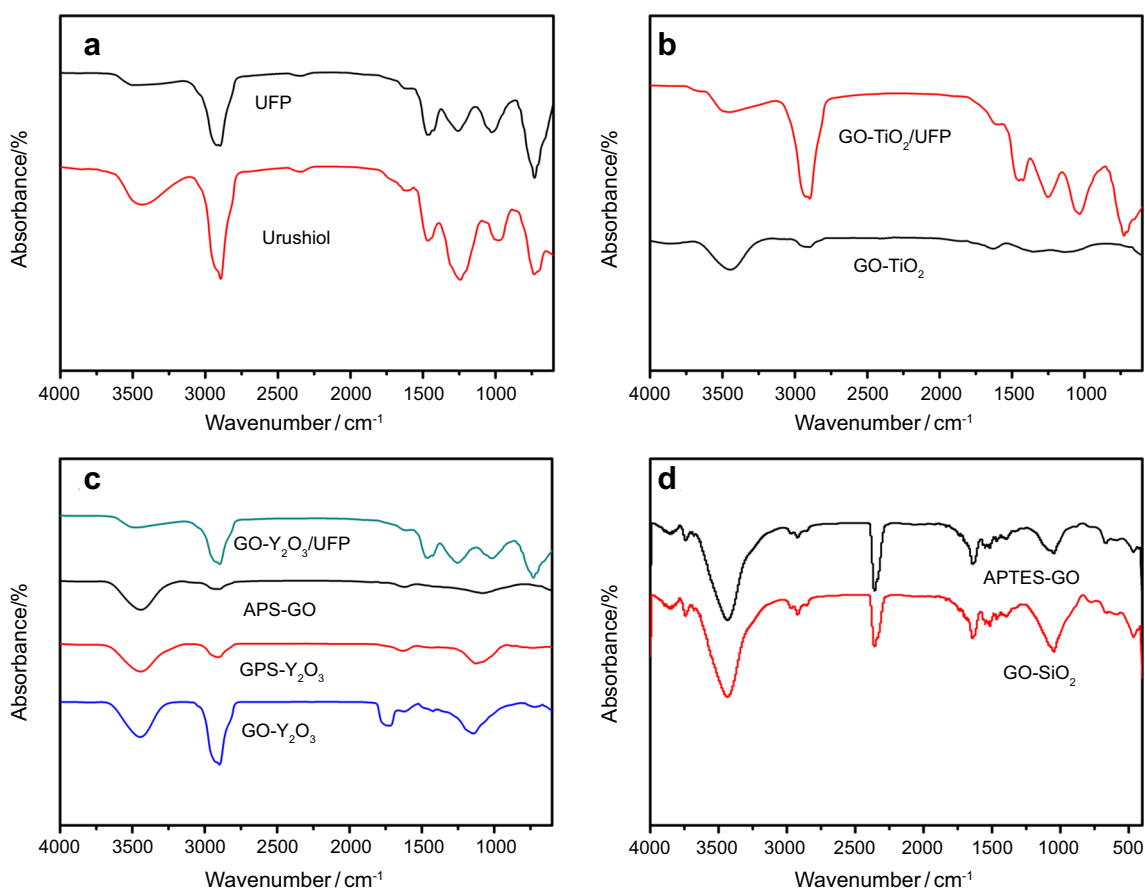**Fig. 4:** FTIR spectra of UFP films and pure urushiol (a), GO–TiO$_2$/UFP films and GO–TiO$_2$ (b), GO–Y$_2$O$_3$/UFP films, APS–GO, GPS–Y$_2$O$_3$ and GO–Y$_2$O$_3$ (c), APTES–GO and GO–SiO$_2$ (d)

observable, including strong bands at 465 and 1100 cm^{-1} assigned to the Si–O–Si bending vibration and the Si–O–C/Si–O–Si asymmetric stretching vibration, respectively, which could be attributed to the chemical reaction between GO and APTES. After APTES-GO reacted with TEOS, three new characteristic peaks appeared at 465 (1090), 694 (1124) and 3260 cm^{-1}. These were attributed to the Si–O–Si bending vibration (asymmetric vibration), Si–O–C stretching and NH$_2$, respectively.[12,37] This suggests that SiO$_2$ was formed on the GO surface through chemical reactions between epoxy and hydrogen groups of GO and the silane coupling agent APTES,[38,39] which was in good accordance with the XPS analysis.

Microstructure and chemical composition of GO–metal oxide in UFP

To evaluate the distribution of GO–Y$_2$O$_3$, GO–TiO$_2$ and GO–SiO$_2$ composites in the UFP matrix, SEM images of the cured UFP composite coatings were also recorded. The SEM micrographs in Fig. 5 show the bulk structural information on the GO–TiO$_2$/UFP, GO–Y$_2$O$_3$/UFP and GO–SiO$_2$/UFP composite films.

Figs. 5a and 5b show the fracture morphology of the GO–TiO$_2$/UFP composite coating. As can be seen in Fig. 5a, GO–TiO$_2$ had a better dispersion performance in UFP at 2 wt%, arising from the composite blending process of GO–TiO$_2$ in UFP, which has been observed to result in thin layers. By contrast, the GO–Y$_2$O$_3$/UFP showed an entirely different fracture morphology. As shown in Figs. 5c and 5d, GO–Y$_2$O$_3$ exhibited a good affinity and compatibility with UFP. There was no obvious aggregation into clusters, and a thin-layered structure was observed instead, which improved the poor dispersion of GO–Y$_2$O$_3$ nanoparticles or the laminar pattern within the UFP polymer. The fractured morphology of the GO–SiO$_2$/UFP composite (Figs. 5e and 5f) showed no visible agglomerations or clusters. In particular, GO–SiO$_2$ was well dispersed in the UFP matrix with a multilayered structure, implying that covalent bonds were formed between the APTES and the GO surface, which was consistent with the structure deduced from the FTIR results. The excellent dispersion could enhance the anticorrosion properties of the UFP coatings, which should be verified in further measurements.
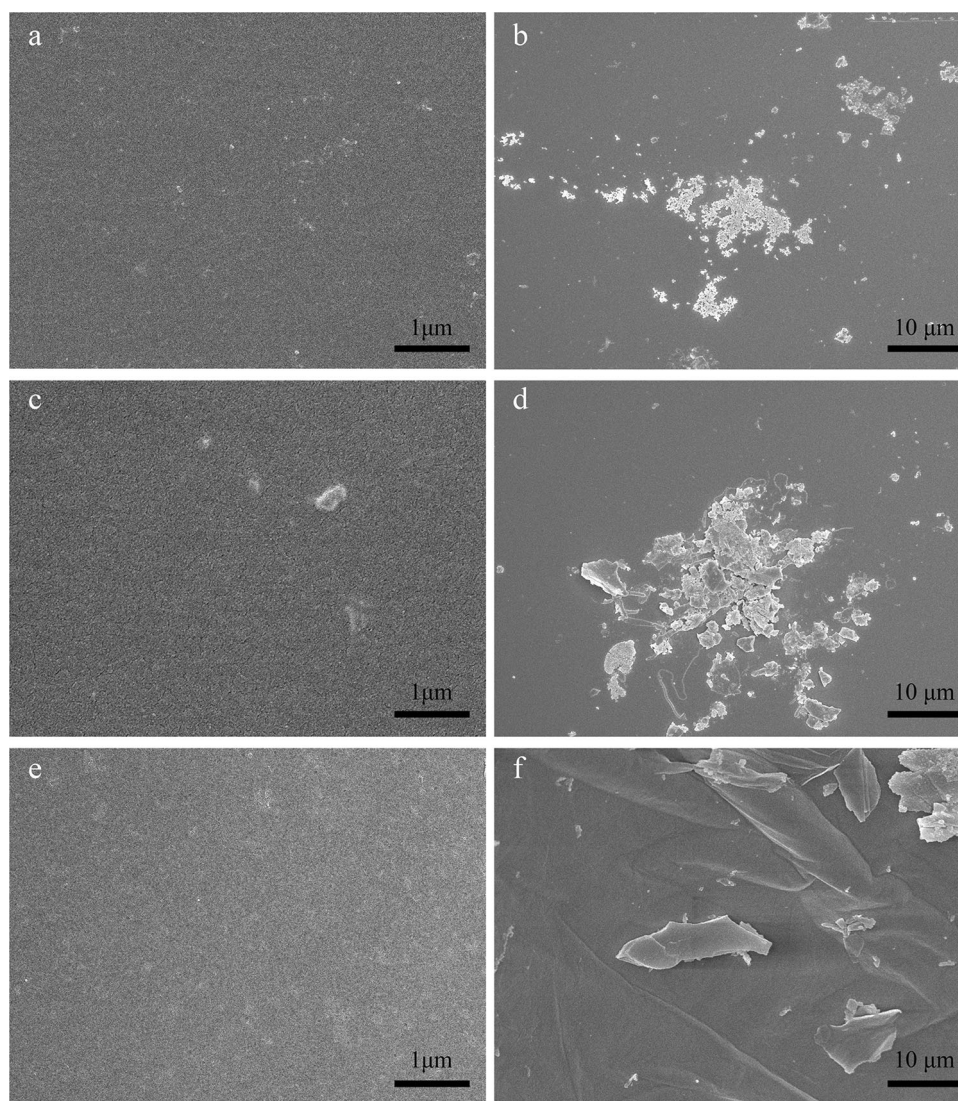
Fig. 5: SEM images of (a) the GO–TiO$_2$/UFP composite coatings, (b) high magnification image of the GO–TiO$_2$/UFP coating, (c) the GO–Y$_2$O$_3$/UFP composite coating, (d) high magnification image of the GO–Y$_2$O$_3$/UFP coating and (e) the GO–SiO$_2$/UFP composite coating, (f) high magnification image of the GO–SiO$_2$/UFP coating on silicon chip substrates

XRD analysis

XRD spectra of GO–TiO$_2$ composite and the GO–TiO$_2$/UFP composite coating are shown in Fig. 6a. In the as-prepared GO–TiO$_2$ samples, a new diminished protuberance was visible at $2\theta = 12.5°$ corresponding to the structure of GO (Fig. 6a), which suggested that the introduction of nano–TiO$_2$ did not destroy the closely packed layered and highly ordered structure of GO.[7,33] The GO–TiO$_2$ wide-angle X-ray diffraction showed a very broad peak at 21.7°, which could indicate that the amorphous GO–TiO$_2$ structure was transformed through APTES.[40] When comparing the pattern of GO–TiO$_2$ with GO–TiO$_2$/UFP, no obvious characteristic diffraction peaks of GO–TiO$_2$ were observed in the XRD pattern of the GO–TiO$_2$/UFP

because the TiO$_2$–GO hybrid nanoparticles were completely dispersed in the UFP matrix.

Figure 6b shows the XRD patterns of APS–GO, GPS–Y$_2$O$_3$, GO–Y$_2$O$_3$ and GO–Y$_2$O$_3$/UFP. According to the Bragg equation [$2d\sin\theta=\lambda$ (λ=0.154 nm)],[33] the interlayer distance of GO (0.80 nm) was larger than that of pristine graphite (0.34 nm) owing to the presence of oxygenated functional groups on the carbon sheets. When comparing the XRD pattern of GO–Y$_2$O$_3$ with that of APS–GO, a small peak is visible around $2\theta = 7.8°$ ($d = 1.13$ nm) in the curve of GO–Y$_2$O$_3$, which can be attributed to GO. The expansion of the interlayer distance of GO confirmed the successful blending process between APS–GO and GPS–Y$_2$O$_3$.[14]

The XRD spectra of APTES–GO, GO–SiO$_2$ and GO–SiO$_2$/UFP are shown in Fig. 6c. Wide-angle X-ray
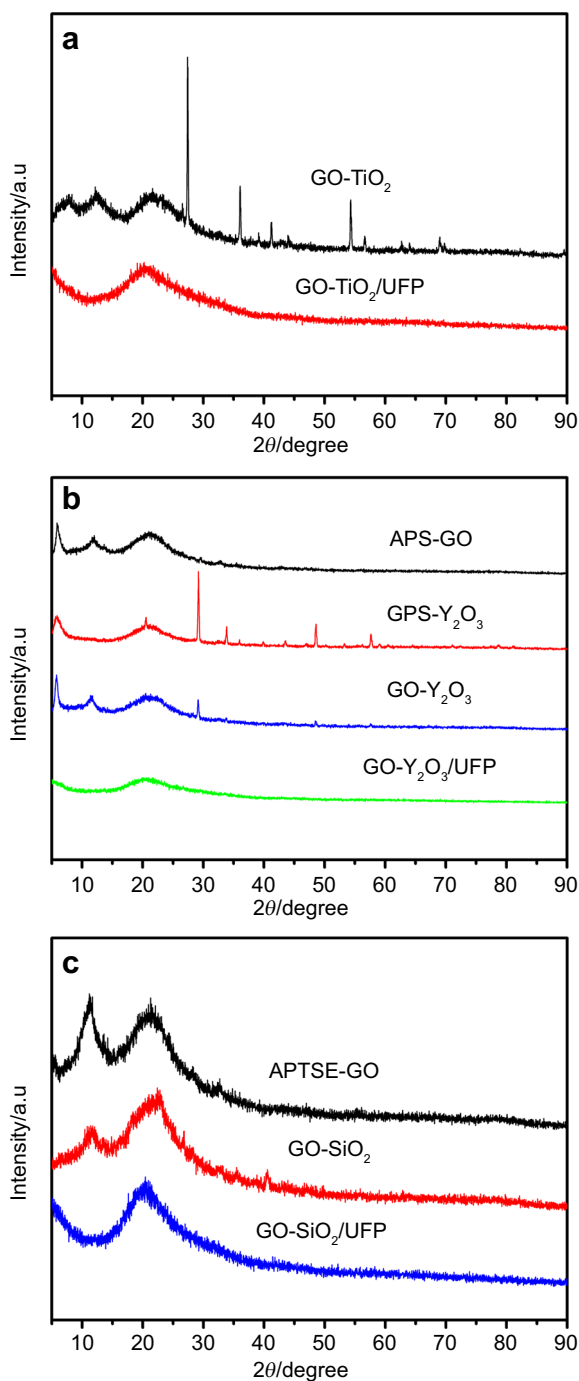
Fig. 6: XRD spectra of GO–TiO₂ and GO–TiO₂/UFP films (a), APS–GO, GPS–Y₂O₃, GO–Y₂O₃ and GO–Y₂O₃/UFP films (b), APTES–GO, GO–SiO₂ and GO–SiO₂/UFP films (c)

diffraction displayed a very broad peak at 19.9° due to the presence of amorphous structure domains in the UFP, which was characteristic of UFP.[41] Figure 6c also shows that the intrinsic diffraction peak of GO was apparently weakened in the GO–SiO₂ and disappeared in the XRD spectrum of the GO–SiO₂/UFP. This means that better dispersion of GO–SiO₂ nanohybrids was achieved in this case.[12]

XPS analysis

To investigate interactions between GO and the metal oxide nanoparticles (TiO_2, Y_2O_3 and SiO_2) as well as the chemical state of the GO-metal oxide composites, XPS was applied to identify the changes in the surface elemental composition of the GO-metal oxide.

The XPS survey results of GO–TiO_2 (a), C 1s (b), O 1s (c), and Ti 2p (d) are shown in Fig. 7. In the XPS survey spectrum of the composite comprising GO–TiO_2 (Fig. 7a), the C 1s spectrum exhibited four peaks located at 284.4, 284.9, 286.6 and 287.9 eV (Fig. 7b), which could be assigned to Ti–O–C, C–C, C–O and C=O, respectively. Observation of Ti–O–C bonding revealed that nano-TiO_2 has been modified by APTES to some extent. The O 1s signals at, respectively, 530.6 and 532.3 eV were associated with two Gauss-Lorentzian peaks related to Ti–O and C–O (Fig. 7c).[42] The Ti 2p, which consisted of peaks at 458.9 and 456.8 eV (Fig. 7d), was related to the Ti 2p1/2 and Ti 2p3/2 core levels of TiO_2, respectively. Taken together, the XPS results indicated that GO was effectively reacted with APTES–TiO_2 to form the surface coating.

The main structural information, including GO–Y_2O_3, N 1s and O 1s, is shown in the XPS survey spectrum (Fig. 8). As can be seen in Fig. 8a, C 1s, O 1s, N 1s, Si 2p and Y 3d were the main signals observed in the XPS spectrum of the GO–Y_2O_3. The O 1s spectrum (Fig. 8b) was separated into five peaks attributed to the binding energies of C–O–C/OH/Si–O–Si (532.8 eV), O=C–O (532.7 eV), C=O/C–O/C–O–Si (532.1 eV), Y–O–Si (531.7 eV) and Y–O (530.6 eV).[14,43] These results indicated that GO and Y_2O_3 were modified by APS and GPS to some degree. The N 1s spectrum of GO–Y_2O_3 in Fig. 8c could be decomposed into two peaks, in which C–N was assigned to 399.1 eV and N–H to 400.4 eV. Based on the results obtained from the XPS analysis, it could be clearly seen that the GPS–Y_2O_3 were grafted onto the APS–GO surface via chemical bonding with two types of functional groups (hydroxyl and carboxylic).

Figure 9 shows wide-scan XPS spectra of GO–SiO_2, whereby peaks in the C 1s, O 1s and Si 2p spectra were detected at binding energies of 283.8, 526.8 and 101.2 eV, respectively. Figure 9b displays the C1s XPS spectrum of GO–SiO_2 with seven peaks appearing at 284.1, 284.7, 285.3, 285.5, 286.7, 288.0 and 289.1 eV. These peaks correspond to the C–Si, C–C/C=C, C–N, C–O/C–O–Si, C–O–C, C=O and O–C=O bonds, respectively, indicating that APTES and TEOS successfully reacted with GO forming chemical bonds with two types of functional groups.[44,45] In addition, the O 1s signals at 530.9, 531.7, 532.3, 532.9 and 533.4 eV were, respectively, related to the five Gauss-Lorentzian peaks of O–C=O, C=O, C–O/C–O–Si, Si–O–Si and C–O–C/OH (Fig. 9c).[46,47] It could be observed that two peaks at 102.5 and 103.4 eV in the Si 2s spectrum (Fig. 9c) were assigned to C–Si and Si–O–Si, respectively, indicating that the GO successfully reacted with
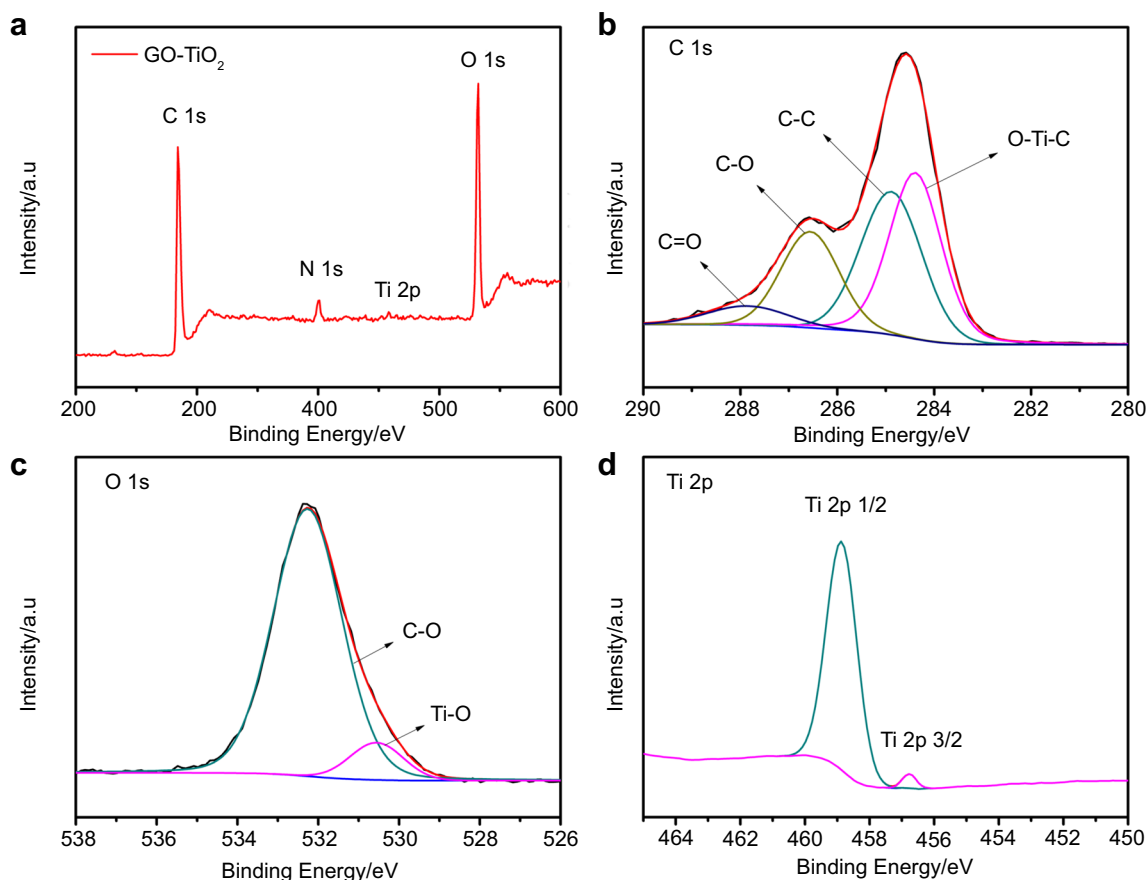
Fig. 7: (a) XPS survey spectrum and high-resolution spectra of GO–TiO$_2$, (b) C 1s, (c) O 1s, and (d) Ti 2p

silane groups, mainly in the form of SiO$_2$ nanoparticles.[44]

As can be seen from Table 1, the Ti 2p, Y 3d and Si 2s signals included 37.12% O–Ti–C, 27.11% Y–O–Si, 23.66% Si–C and 76.34% Si–O–Si peaks, which indicated that most of the silane moieties could be successfully grafted onto the GO surface via chemical bonding in the formation of the UFP composite coatings. Importantly, the results were in good agreement with the FTIR analysis described above.[33,48]

Electrochemical tests

For better understanding and to judge the corrosion stage, the Nyquist and Bode plots were fitted with proper equivalent electrical circuits as shown in Fig. 10. The EIS fitted results were indicative of the two different stages of the corrosion process (the initial and terminal stages). In the equivalent electrical circuits, the elements contain the electrolyte resistance (R_s), coating capacitance (C_c), and coating resistance (R_c), respectively.

Potentiodynamic analysis

The anticorrosive properties of the three UFP composite coatings were estimated using the potentiodynamic polarization analysis.[37,49] Figure 11 shows the Tafel plots of tinplates with and without coatings (GO–SiO$_2$/UFP, GO–TiO$_2$/UFP and GO–Y$_2$O$_3$/UFP) in 3.5% NaCl after soaking for 18 d. The electrochemical parameters from the polarization curves were obtained and listed in Table 2. According to the polarization curves, the samples coated with GO–TiO$_2$/UFP displayed more negative corrosion potentials (E_c, −461.48 mV) and significantly lower corrosion current densities (i_c, 1.86×10^{-9} A/cm^2). By contrast, the GO–Y$_2$O$_3$/UFP-coated tinplate substrate exhibited a more positive E_c (−374.82 mV vs SCE), with a significant increase of i_c (1.29×10^{-8} A/cm^2). However, the corrosion rate (C.R., 2.18×10^{-5} mm/a) and corrosion protection efficiency (P.E., 99.59%) of the GO–TiO$_2$/UFP composite coatings were significantly changed by the reduction of i_c accompanied by a more positive E_c due to the addition of GO–TiO$_2$.[49] These results indicated that the GO–TiO$_2$/UFP coating provided better corrosion protection to the metal substrate than other UFP composite coatings and effectively decreased the corrosion rate of the tinplate. Thus, the anticorrosion
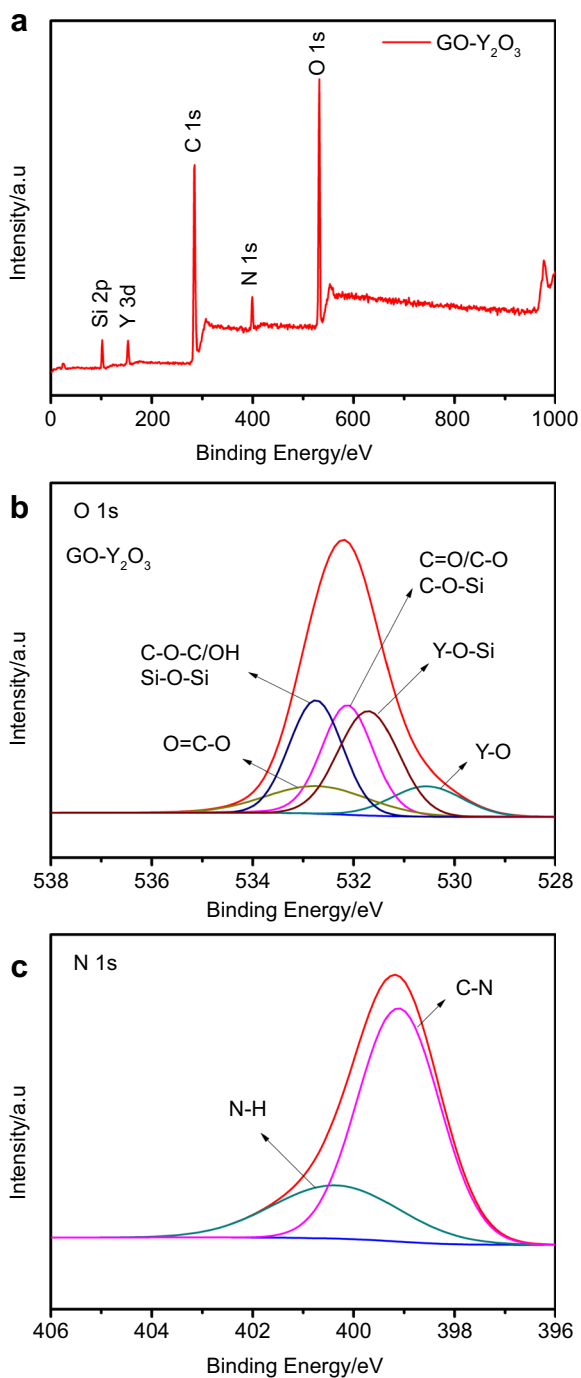
Fig. 8: (a) XPS survey spectrum and high-resolution spectra of GO–Y$_2$O$_3$, (b) O 1s, and (c) N 1s

properties of the GO–TiO$_2$/UFP composite coating were improved by adding GO–TiO$_2$, especially due to its good distribution within the UFP matrix,[50] which further reinforced the composite's anticorrosion performance. Well-dispersed GO–TiO$_2$ embedded in UFP matrix provided a superior barrier effect due to its two-dimensional sheet structure and plugging inherent

micropores properties, thereby exhibiting superior corrosion protection to the metals.

In this study, the protection efficiency (P.E.) and corrosion rate (C.R.) of composite coatings were used to better understand the corrosion process of metal substrates coated with the UFP composite coatings. The corresponding values were calculated based on equations (1)[53] and (2),[51,52] respectively.

$$C.R. = 3.27 \times 10^{-3} \times \frac{i_{corr}}{\rho} \times E_w \qquad (1)$$

$$P.E.(\%) = (I_0 - I_c/I_0) \times 100 \qquad (2)$$

In equation (1), E_W is the equivalent weight of the tinplate (4.01 g) and ρ is the density of the tinplate (7.85 g/cm^3). In equation (2), I_0 (μA/cm^2) is the corrosion current of the neat tinplate, while I_c (μA/cm^2) is the corrosion current of the tinplate coated with the UFP composite coating. The parameters extracted from the polarization curves were in good agreement with the electrochemical tests (Table 2).

EIS measurements of the composite coatings

The electrochemical impedance spectroscopy (EIS) measurements of the different GO-metal oxide/UFP composite coatings were displayed in the form of the Nyquist plots and Bode diagrams. In addition, the EIS fitted data with suitable electrically equivalent circuits were also shown in the figures for comparison (solid lines). The determination of the corrosion stage plays a key role in the study of corrosion processes. In the initial stage of the corrosion process, the electrolyte solution penetrated into the coating through inherent micropores. In the middle stage, the corrosion reaction occurred. The terminal stage comprises a diffusion process, but UFP polymer wearing is nonconspicuous.[53–56]

Figures 12 and 14 show the Bode and Nyquist plots of GO–SiO$_2$/UFP, GO–TiO$_2$/UFP and GO–Y$_2$O$_3$/UFP composite coatings after immersion for 2 and 16 days, respectively.

Figures 12a and 12b, respectively, showed the Nyquist and Bode plots of the GO–SiO$_2$/UFP, GO–TiO$_2$/UFP and GO–Y$_2$O$_3$/UFP coatings after 2 days of immersion in 3.5% NaCl solution. The radius of the impedance arc of the GO–TiO$_2$/UFP composite coating was significantly higher than that of the other two composite coatings; the impedance modulus at the low frequency for GO–SiO$_2$/UFP, GO–TiO$_2$/UFP and GO–Y$_2$O$_3$/UFP coatings was 1.62×10^8, 1.27×10^{10} and 4.14×10^8 Ω cm^2, respectively. Signals at the larger radius of the impedance arc correspond to greater anticorrosion resistance and more difficult electron transfer,[37,57] whereby the GO–TiO$_2$/UFP composite coating exhibited a significantly higher value than both GO–SiO$_2$/UFP and GO–Y$_2$O$_3$/UFP.
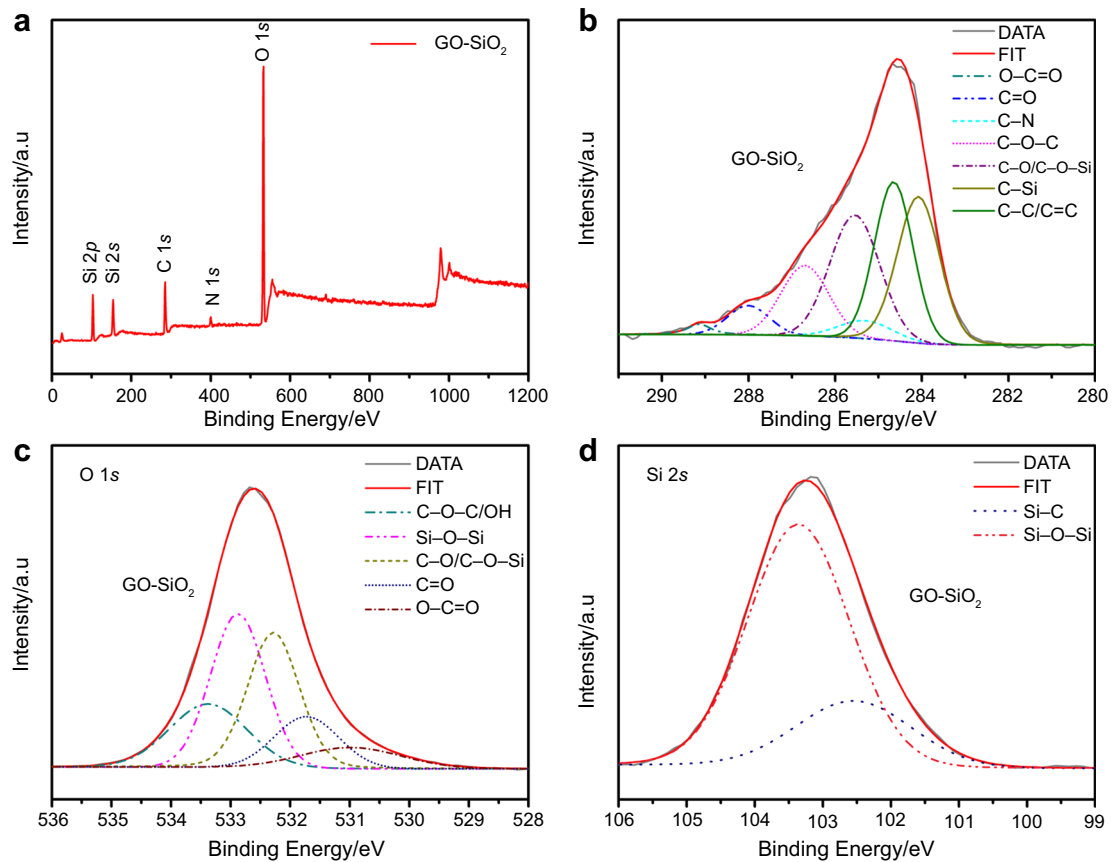
Fig. 9: (a) XPS survey spectrum and high-resolution spectra of GO–SiO$_2$, (b) C 1s, (c) O 1s, and (d) Si 2s

Table 1: The XPS results for the GO–TiO$_2$, GO–Y$_2$O$_3$ and GO–SiO$_2$ sample

Signal	Bond	Energy of bonds/eV	Components/%
O 1s	Y–O–Si	531.7	27.11
C 1s	O–Ti–C	284.4	37.12
Si 2s	Si–O–Si	103.4	76.34
Si 2s	Si–C	102.5	23.66
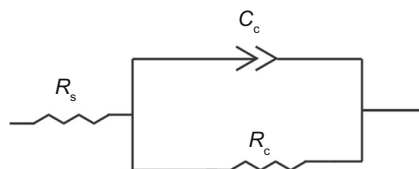
Fig. 10: The proposed equivalent circuit used to fit the EIS experimental data

Fig. 11: Potentiodynamic polarization curves for the GO–TiO$_2$/UFP, GO–Y$_2$O$_3$/UFP and GO–SiO$_2$/UFP composite coatings on tinplate substrates after immersion in 3.5% NaCl solution for 18 days

According to Figs. 12a and 12b, one time constant appeared in initial state, which indicated that the corrosion process did not occur, and these three coatings displayed excellent barrier properties. In addition, in Bode plots o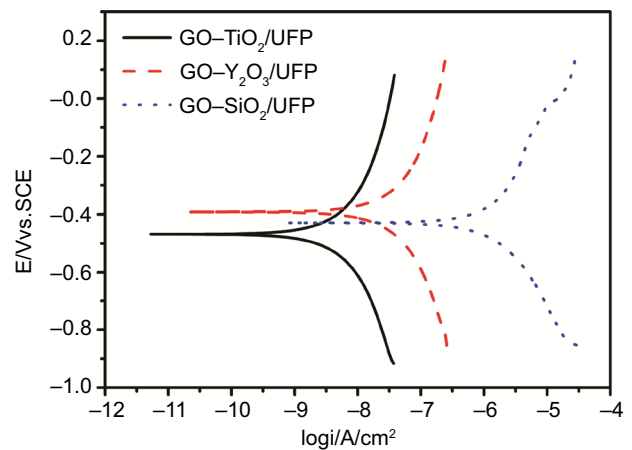f the three composite coatings, the phase angle of the GO–TiO$_2$/UFP composite coatings could reach more − 90° of the highest value (Fig. 12b) even after immersing for 2 days, which indicated that the GO–TiO$_2$/UFP composite coatings had pronounced anticorrosive properties. This indicated that incorporation of GO–TiO$_2$ is a promising approach for

Table 2: Electrochemical parameters obtained from the polarization curves of the UFP coatings containing different contents of GO–TiO$_2$, GO–Y$_2$O$_3$, GO–SiO$_2$ and MGO

Sample	Composite	E_c/mV	i_c/A/cm^2	R_c/KΩ/cm^2	i_o/A/cm^2	CR/mm/a	PE/%
1	GO–TiO$_2$	− 461.48	1.86E−09	1.40×10^4	4.54E−07	2.18×10^{-5}	99.59
2	GO–Y$_2$O$_3$	− 374.82	1.29E−08	2.02×10^3	4.54E−07	1.52×10^{-4}	97.15
3	GO–SiO$_2$	− 400.34	1.08E−08	24.14	4.54E−07	1.27×10^{-2}	97.62
4	MGO	− 414.91	2.49E−09	1.05×10^4	4.54E−07	2.93×10^{-5}	99.45
5	UFP	− 509.80	3.73E−08	7.00×10^2	4.54E−07	4.39×10^{-4}	91.79

Fig. 12: Nyquist (a) and Bode (b) plots of UFP coatings corresponding to GO–TiO$_2$/UFP, GO–Y$_2$O$_3$/UFP and GO–SiO$_2$/UFP after 2 days of immersion in 3.5% NaCl solution; the marker points and solid lines show the experimental and fitted data, respectively
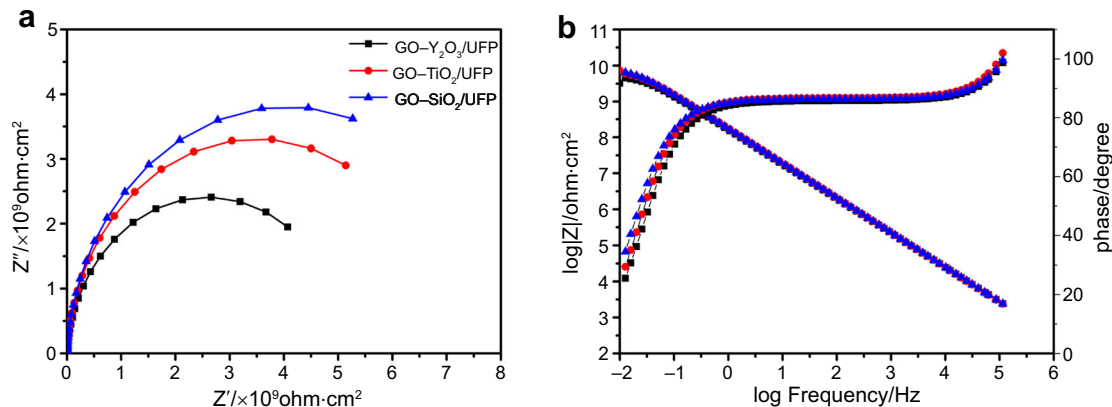

Fig. 13: Nyquist (a) and Bode (b) plots of UFP coatings corresponding to GO–TiO$_2$/UFP, GO–Y$_2$O$_3$/UFP and GO–SiO$_2$/UFP after 16 days of immersion in a 3.5% NaCl solution; the marker points and solid lines show the experimental and fitted data, respectively
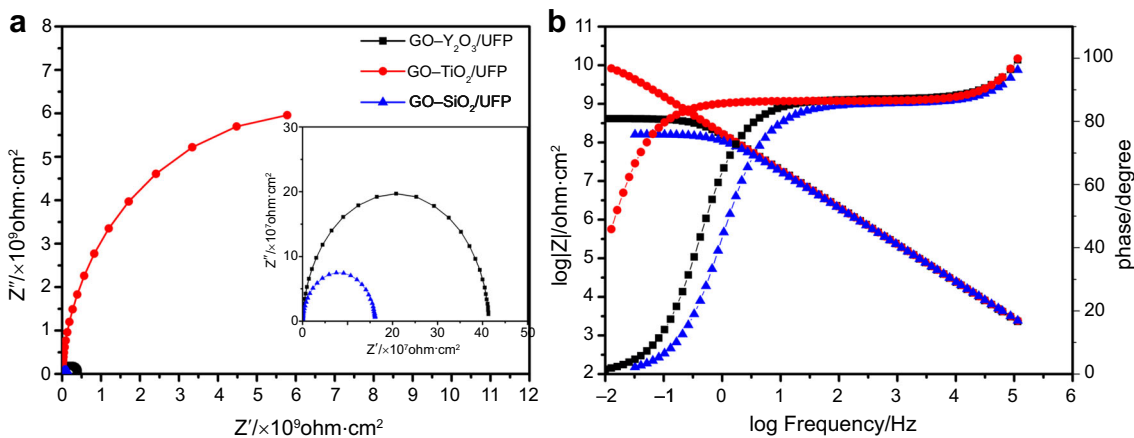
improving the barrier properties of the UFP coatings at initial immersion. The corresponding phase angle of the GO–TiO$_2$/UFP composite coating was the highest among the three UFP composite coatings, which was another clear sign of the improved corrosion resistance of GO–TiO$_2$/UFP composite coatings.

Figures 13a and 13b showed the Nyquist and Bode plots of the GO–SiO$_2$/UFP, GO–TiO$_2$/UFP and GO–Y$_2$O$_3$/UFP composite coatings. GO–TiO$_2$/UFP maintained a relatively high modulus and phase angle, which may be attributed to the GO–TiO$_2$ hybrid nanoparticles, including their two-dimensional structure and uniform dispersion properties. Accordingly, it
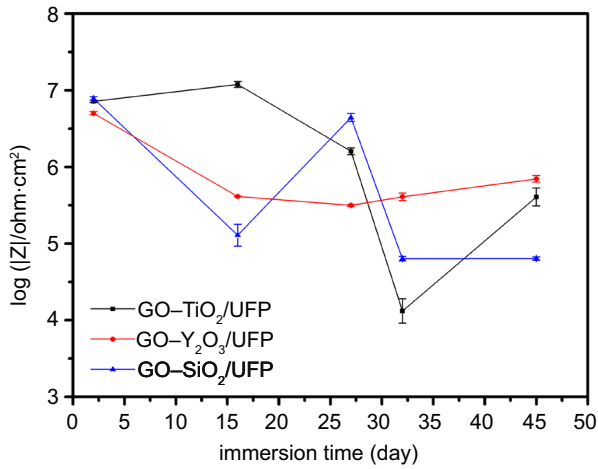
Fig. 14: The variation of the $|Z|_{0.01\ Hz}$ value versus immersion time in a 3.5% NaCl solution for GO–TiO$_2$/UFP, GO–Y$_2$O$_3$/UFP and GO–SiO$_2$/UFP samples

was confirmed that the GO–TiO$_2$ composite coating remarkably improved the corrosion resistance of the UFP coating.

The variation of the $|Z|$0.01 Hz values of the GO–metal oxide/UFP samples vs immersion time is shown in Fig. 14. The $|Z|$0.01 Hz values of the GO–TiO$_2$/UFP composite coating were higher than those of the two other samples during the immersion, indicating a better corrosion protection performance of the GO–TiO$_2$/UFP composite coating due to the barrier effect of the GO–TiO$_2$ in the UFP polymer. The impedance values decreased for all UFP composite coatings with the increase of immersion time. It suggested that the corrosive electrolyte gradually diffused into the coating, thereby increasing the porosity and presence of electrolyte pathways.[12] Obviously, these results were in good accordance with the electrochemical tests.

According to Table 3, the GO–TiO$_2$/UFP coating had higher R_c than the other two samples. Indeed, the R_c values of the UFP composite coatings decreased with prolonged immersion time in the order of UFP < GO–SiO$_2$/UFP < GO–Y$_2$O$_3$/UFP < GO–TiO$_2$/UFP. The increase of the R_c value indicated the good dispersion of GO–TiO$_2$ in the coating, which improved its resistance against the uptake of corrosive species by decreasing its porosity.[58,59]

Chemical resistance of the UFP composite coatings

To demonstrate the superior alkali resistance of the GO–SiO$_2$/UFP, GO–TiO$_2$/UFP and GO–Y$_2$O$_3$/UFP composite coatings, the chemical resistance of the coatings was examined by immersing coated samples in 10% NaOH, 30% H$_2$SO$_4$ and 3% NaCl for up to 14 days at room temperature, in conjunction with visual observations for cracking, blistering or other signs of solvent attack on the coatings surface. The results of the chemical resistance tests conducted on the com-

Table 3: Electrochemical parameters obtained from the EIS spectra of the UFP coatings containing different contents of GO–TiO$_2$, GO–Y$_2$O$_3$ and GO–SiO$_2$

Sample	Composite	R_c/KΩ/cm^2	CPE1	
			Y_1/$\mu\Omega^{-1}m^{-2}S^n$	n_1
1	GO–TiO$_2$	1.27E+07	9.86E–04	0.96085
2	GO–Y$_2$O$_3$	4.14E+05	9.33E–04	0.96761
3	GO–SiO$_2$	1.62E+05	1.09E–03	0.95254

posite coatings are listed in Table 4 as a reference for the electrochemical impedance spectroscopy (EIS) data. The GO–SiO$_2$/UFP showed a better alkali resistance than the other UFP composite coatings, with no damage after 14 days of immersion in a 10% NaOH solution, which indicated that the alkali resistance could be improved via the chemical reaction between GO–SiO$_2$ and UFP by decreasing the hydroxyl group content of pure UFP coating.[1]

Corrosion protection mechanism

An explanation of the corrosion-resistance mechanisms of the GO–metal oxide/UFP composite coating was proposed according to the preceding observations and analysis.

Based on the coating capacitance [equations (3) and (5)][60–62] and the Brasher–Kingsbury equation [equation (4)], it was assumed that the transport of water through the polymer coating follows Fick's law:[63,64]

$$C_c = \varepsilon\varepsilon_0 A/d \tag{3}$$

$$\phi_w = \frac{\log \frac{C_c}{C_0}}{\log \varepsilon_w} \tag{4}$$

$$C_c = (Y_0)^{\frac{1}{n}} \cdot (R_{pore})^{\frac{1-n}{n}} \tag{5}$$

In equation (3), A is the active area, d is the coating thickness, ε is the relative dielectric constant of the UFP composite coating and ε_0 the permittivity of vacuum (8.85×10^{-14} F cm^{-1}). In equation (4), ε_w is the dielectric constant of water ($\varepsilon_w \approx 80$), C_c is the coating capacitance at immersion time t, and C_0 is the initial capacitance of the dry coating. The volume fraction of water uptake (φ_w) in the GO–TiO$_2$/UFP coatings can be calculated from their capacitance (C_c). In equation (5), the coating capacitance value was obtained using the EIS method including the admittance parameter (Y_0) and an exponent (n). The constant phase element consisting of the two parameters represented the deviation from ideal capacitive behavior. According to equation (4), this showed that the effect of an increase of the dielectric constant with

Table 4: Resistance of the GO–TiO$_2$/UFP, GO–Y$_2$O$_3$/UFP and GO–SiO$_2$/UFP composite coatings against chemical attack after immersion in 30% H$_2$SO$_4$, 10% NaOH and 3% NaCl solution at room temperature

Sample	Composition		Chemical medium		
			30% H$_2$SO$_4$	10% NaOH	3% NaCl
1	GO–Y$_2$O$_3$	UFP	+	+	+
2	GO–TiO$_2$	UFP	+	+	+
3	GO–SiO$_2$	UFP	+	+	+
4	UFP		-	-	-

the permeation of water may increase the C_c value. That is, a change of the capacitance value indicates water uptake via the GO–metal oxide/UFP polymer film. In the case of the GO–TiO$_2$/UFP sample, corrosive electrolytes diffused into the coating increasing the amount of water uptake. Subsequently, crosslinking density of the UFP composite coating contributed to the significant decrease in the amount of water uptake with increasing immersion time. This indicated that silanols reacted with UFP by hydrolysis and condensation. It could be confirmed that the electrochemical corrosion resistance of the GO–TiO$_2$/UFP composite coating was superior to that of the other GO–metal oxide/UFP materials since GO–TiO$_2$ served as a barrier that blocked the diffusion paths of corrosive agents.

It is not difficult to see that the protection efficiency (P.E.) of the GO–TiO$_2$/UFP coatings increased remarkably by adding 3.0 wt% GO–TiO$_2$, which serves to demonstrate that the GO–TiO$_2$/UFP composite coating exhibited anticorrosive properties of metallic substrates by making the diffusion pathways of corrosive agents in the UFP more tortuous.[65,66] According to a few reports, the atomic/molecular situation of the interface of metal and organic coatings was assessed based on QM (quantum mechanics) approaches.[69] The QM computations also evidenced that with increasing the amino groups bound to GO surface, the interactions of UFP with modified GO surface strengthened, which could result in improved properties of prepared coatings of UFP and modified GO. Inclusion of GO–SiO$_2$, GO–TiO$_2$ and GO–Y$_2$O$_3$ into the UFP coating improved its anticorrosion properties. The highest improvement of the polymer barrier performance was seen in the case of GO–TiO$_2$ composites. As a result, owing to stronger interfacial interactions, a metal substrate with higher OH coverage will be coated with a thicker cured-UFP layer, which leads to enhanced protection of carbon steel.[67–70] Accordingly, a corrosion protection mechanism for GO–TiO$_2$/UFP composite coatings could be proposed as shown in Fig. 15.
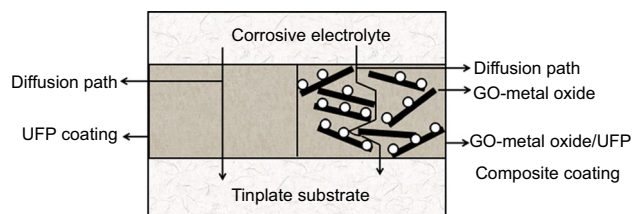
Fig. 15: Schematic representation of the most likely mechanism of corrosion protection by the GO–metal oxide/UFP composite coatings on tinplate substrates

Conclusions

Metal oxide nanoparticle-decorated graphene oxide composites (GO–SiO$_2$, GO–TiO$_2$ and GO–Y$_2$O$_3$) were synthesized via a simple two-step solution approach. Their structure and morphology were characterized and they were incorporated into UFP-based coatings. The corrosion-resistance properties of the GO–metal oxide/UFP composite coatings were investigated by various techniques. The main findings are as follows: (1) Compared with the two other GO–metal oxide composites, the dispersion, compatibility, barrier properties and corrosion resistance of the GO–TiO$_2$/UFP composite coating were dramatically enhanced. (2) The addition of GO–SiO$_2$ appears to be an appropriate approach to evidently improve the alkali resistance of UFP at low doses. At 0.1 wt% and above, the addition of GO–SiO$_2$ drastically increased the alkali resistance of the resulting GO–SiO$_2$/UFP composite coating due to the chemical reaction between GO–SiO$_2$ and UFP, providing a more effective barrier against the ingress of corrosive ions.

References

1. Bai, WB, Lin, JH, "Characterisation of urushiol formaldehyde polymer/multihydroxyl polyacrylate/SiO$_2$ nanocompos-

ites prepared by the sol–gel method.'' *Prog. Org. Coat.,* **71** 43–47 (2011)

2. Xu, YL, Tong, ZQ, Xia, JR, Hu, BH, Lin, JH, ''Urushiol-formaldehyde polymer microporous films with acid-alkali resistance property: Effects of formation conditions on surface morphologies.'' *Prog. Org. Coat.,* **72** 586–591 (2011)

3. Kim, HW, Miura, Y, Macosko, CW, ''Graphene/polyurethane composites for improved gas barrier and electrical conductivity.'' *Chem. Mater.,* **22** 3441–3450 (2010)

4. Tang, J, Yao, W, Li, W, Xu, J, Jin, L, Zhang, J, Xu, Z, ''Study on a novel composite coating based on PDMS doped with modified graphene oxide.'' *J. Coat. Technol. Res.,* **15** 375–383 (2018)

5. Carrasco-Valenzuela, L, Zaragoza-Contreras, EA, Vega-Rios, A, ''Synthesis of graphene oxide/poly (3,4–ethylenedioxythiophene) composites by Fenton's reagent.'' *Polymer,* **130** 124–134 (2017)

6. Ma, HX, Xu, ZB, Qiu, JJ, Liu, CM, ''Synthesis of artificial urushi via ring-opening reaction of benzoxazine with renewable cardanol.'' *Polymer,* **132** 41–50 (2017)

7. He, LH, Zhao, Y, Xing, LY, Liu, PG, Wang, ZY, Zhang, YW, Liu, XF, ''Preparation of phosphonic acid functionalized graphene oxide-modified aluminum powder with enhanced anticorrosive properties.'' *Appl. Surf. Sci.,* **411** 235–239 (2017)

8. Botas, C, Álvarez, P, Blanco, P, Granda, M, Blanco, C, Santamaría, R, Romasanta, LJ, Verdejo, R, López-Manchado, MA, Menéndez, R, ''Graphene materials with different structures prepared from the same graphite by the Hummers and Brodie methods.'' *Carbon,* **65** 156–164 (2013)

9. Srinivas, G, Zhu, Y, Piner, R, Skipper, N, Ellerby, M, Ruoff, R, ''Synthesis of graphene-like nanosheets and their hydrogen adsorption capacity.'' *Carbon,* **48** 630–635 (2010)

10. Navalon, S, Dhakshinamoorthy, A, Alvaro, M, Garcia, H, ''Carbocatalysis by graphene-based materials.'' *Chem. Rev.,* **114** 6179–6212 (2014)

11. Qian, R, Yu, J, Wu, C, Zhai, X, Jiang, P, ''Alumina-coated graphene sheet hybrids for electrically insulating polymer composites with high thermal conductivity.'' *RSC Adv.,* **3** 17373–17379 (2013)

12. Ramezanzadeh, B, Haeri, Z, Ramezanzadeh, M, ''A facile route of making silica nanoparticles-covered graphene oxide nanohybrids (SiO$_2$–GO); fabrication of SiO$_2$–GO/epoxy composite coating with superior barrier and corrosion protection performance.'' *Chem. Eng. J.,* **303** 511–528 (2016)

13. Jiang, G, Lin, Z, Chen, C, Zhu, L, Chang, Q, Wang, N, ''TiO$_2$ nanoparticles assembled on grapheme oxide nanosheets with high photocatalytic activity for removal of pollutants.'' *Carbon,* **49** 2693–2701 (2011)

14. Lei, P, Leroy, W, Dai, B, Zhu, JQ, Chen, XT, Han, JC, Depla, D, ''Study on reactive sputtering of yttrium oxide: Process and thin film properties.'' *Surf. Coat. Technol.,* **276** 39–46 (2015)

15. Yu, Z, Di, H, Ma, Y, He, Y, Lianf, L, Lv, L, Ran, X, Pan, Y, Luo, Z, ''Preparation of graphene oxide modified by titanium dioxide to enhance the anti-corrosion performance of epoxy coatings.'' *Surf. Coat. Technol.,* **276** 471–478 (2015)

16. Yu, Z, Di, H, Ma, Y, Lv, L, Pan, Y, Zhang, C, He, Y, ''Fabrication of graphene oxide-alumina hybrids to reinforce the anti-corrosion performance of composite epoxy coatings.'' *Appl. Surf. Sci.,* **351** 986–996 (2015)

17. Williams, G, Kamat, PV, ''Graphene–semiconductor nanocomposites: Excited-state interactions between ZnO nanoparticles and graphene oxide.'' *Langmuir,* **25** 13869–13873 (2009)

18. Wang, CX, Mao, HY, Wang, CX, Fu, SH, ''Dispersibility and hydrophobicity analysis of titanium dioxide nanoparticles grafted with silane coupling agent.'' *Ind. Eng. Chem. Res.,* **50** 11930–11934 (2011)

19. Shao, L, Quan, S, Liu, Y, Guo, Z, Wang, Z, ''A novel gel–sol strategy to synthesize TiO$_2$ nanorod combining reduced graphene oxide composites.'' *Mater. Lett.,* **107** 307–310 (2013)

20. Tatou, M, Genix, AC, Imaz, A, Forcada, J, Banc, A, Schweins, R, ''Reinforcement and polymer mobility in silica-latex nanocomposites with controlled aggregation.'' *Macromolecules,* **44** 9029–9039 (2011)

21. Emamgholizadeh, A, Omrani, A, Rostami, AA, Rostami, A, ''Corrosion protection of steel 316 using coatings based on epoxy and poly p-phenylendiamine-SiO$_2$ nanocomposite.'' *Chem. Eng. Commun.,* **202** 1389–1396 (2015)

22. Jiang, T, Kuila, T, Kim, NH, Ku, BC, Lee, JH, ''Enhanced mechanical properties of silanized silica nanoparticle attached graphene oxide/epoxy composites.'' *Compos. Sci. Technol.,* **79** 115–125 (2013)

23. Palraj, S, Selvaraj, M, Maruthan, K, Rajagopal, G, ''Corrosion and wear resistance behavior of nano-silica epoxy composite coatings.'' *Prog. Org. Coat.,* **81** 132–139 (2015)

24. Bakhshandeh, E, Jannesari, A, Ranjbar, Z, Sobhani, S, Saeb, MR, ''Anti-corrosion hybrid coatings based on epoxy-silica nano-composites: Toward relationship between the morphology and EIS data.'' *Prog. Org. Coat.,* **77** 1169–1183 (2014)

25. Courcot, E, Rebillat, F, Teyssandier, F, Louchet-Pouillerie, C, ''Stability of rare earth oxides in a moist environment at elevated temperatures-experimental and thermodynamic studies: Part II: Comparison of the rare earth oxides.'' *J. Eur. Ceram. Soc.,* **30** 1911–1917 (2010)

26. de Rouffignac, P, Park, JS, Gordon, RG, ''Atomic layer deposition of Y$_2$O$_3$ thin films from yttrium tris(N,N′-diisopropylacetamidinate) and water.'' *Chem. Mater.,* **17** 4808–4814 (2005)

27. Aghazadeh, M, Barmi, AAM, Shiri, HM, ''Cathodic electrodeposition and characterization of nanostructured Y$_2$O$_3$ from chloride solution Part I: Effect of current density.'' *Russ. J. Electrochem.,* **49** 344–353 (2013)

28. Barve, SA, Mithal, N, Deo, MN, Biswas, A, Mishra, R, Kishore, R, Bhanage, BM, Gantayet, LM, Patil, DS, ''Effects of precursor evaporation temperature on the properties of the yttrium oxide thin films deposited by microwave electron cyclotron resonance plasma assisted metal organic chemical vapor deposition.'' *Thin Solid Films,* **519** 3011–3020 (2011)

29. Di, H, Yu, Z, Ma, Y, Zhang, C, Li, F, Lv, L, Pan, Y, Shi, H, He, Y, ''Corrosion-resistant hybrid coatings based on graphene oxide-zirconia dioxide/epoxy system.'' *J. Taiwan Inst. Chem. Engrs.,* **67** 511–520 (2016)

30. Marks, JG, Demelfi, T, Mccarthy, MA, Witte, EJ, Castagnoli, N, Epstein, WL, Aber, RC, ''Dermatitis from cashew nuts.'' *J. Am. Acad. Dermatol.,* **10** 627–631 (1984)

31. Li, F, Liu, Y, Qu, CB, Xiao, HM, Hua, Y, Sui, GX, Fu, SY, ''Enhanced mechanical properties of short carbon fiber reinforced polyethersulfone composites by graphene oxide coating.'' *Polymer,* **59** 155–165 (2015)

32. Chiong, SJ, Goh, PS, Ismail, AF, ''Novel hydrophobic PVDF/APTES-GO nanocomposite for natural gas pipelines coating.'' *J. Nat. Gas Sci. Eng.,* **42** 190–202 (2017)

33. Haeri, SZ, Ramezanzadeh, B, Asghari, M, ''A novel fabrication of a high performance SiO$_2$-graphene oxide (GO) nanohybrids: Characterization of thermal properties of epoxy nanocomposites filled with SiO$_2$–GO nanohybrids.'' *J. Colloid Interface Sci.,* **493** 111–122 (2017)

34. Ahmadi-Moghadam, B, Sharafimasooleh, M, Shadlou, S, Taheri, F, "Effect of functionalization of graphene nanoplatelets on the mechanical response of graphene/epoxy composites." *Mater. Des.,* **66** 142–149 (2015)

35. Wu, YY, He, D, Zhang, H, Li, S, Liu, XP, Wang, SM, Jiang, LJ, "Preparation of yttrium oxide coating by MOCVD as tritium permeation barrier." *Fusion Eng. Des.,* **90** 105–109 (2015)

36. He, F, Fan, J, Ma, D, Zhang, L, Leung, C, Chan, HL, "The attachment of Fe_3O_4 nanoparticles to graphene oxide by covalent bonding." *Carbon,* **48** 3139–3144 (2010)

37. Pourhashem, S, Vaezi, MR, Rashidi, A, "Investigating the effect of SiO_2-graphene oxide hybrid as inorganic nanofiller on corrosion protection properties of epoxy coatings." *Surf. Coat. Technol.,* **311** 282–294 (2017)

38. Yang, H, Li, F, Shan, C, Han, D, Zhang, Q, Niu, L, Ivaska, A, "Covalent functionalization of chemically converted graphene sheets via silane and its reinforcement." *J. Mater. Chem.,* **19** 4632–4638 (2009)

39. Zhang, WL, Choi, HJ, "Silica-graphene oxide hybrid composite particles and their electroresponsive characteristics." *Langmuir,* **28** 7055–7062 (2012)

40. Kumar, M, Gholamvand, Z, Morrissey, A, Nolan, K, Ulbricht, M, Lawler, J, "Preparation and characterization of low fouling novel hybrid ultrafiltration membranes based on the blends of GO–TiO_2 nanocomposite and polysulfone for humic acid removal." *J. Membr. Sci.,* **506** 38–49 (2016)

41. Sato, S, Ido, R, Ose, T, Takahashi, Y, Kanehashi, S, Ishimura, T, Honda, T, Miyakoshi, T, Nagai, K, "Transformation of a Kurome natural lacquer film from glassy to rubbery polymer by the presence of moisture." *Prog. Org. Coat.,* **104** 43–49 (2017)

42. Zhu, ZY, Zhou, F, Zhan, S, Tian, Y, He, QC, "Study on the bactericidal performance of graphene/TiO_2 composite photocatalyst in the coating of PEVE." *Appl. Surf. Sci.,* **430** 116–124 (2018)

43. Zhu, JQ, Zhu, YK, Shen, WX, Wang, YJ, Han, JC, Tian, G, Lei, P, Dai, B, "Growth and characterization of yttrium oxide films by reactive magnetron sputtering." *Thin Solid Films,* **519** 4894–4898 (2011)

44. Zhi, MY, Huang, WX, Shi, QW, Ran, K, "Improving water dispersibility of non-covalent functionalized reduced graphene oxide with L-tryptophan via cleaning oxidative debris." *J. Mater. Sci. Mater. Electron.,* **7** 7361–7368 (2016)

45. Haeri, SZ, Asghari, M, Ramezanzadeh, B, "Enhancement of the mechanical properties of an epoxy composite through inclusion of graphene oxide nanosheets functionalized with silica nanoparticles through one and two steps sol-gel routes." *Prog. Org. Coat.,* **111** 1–12 (2017)

46. Tzeng, P, Stevens, B, Devlaming, I, Grunlan, JC, "Polymer-graphene oxide quadlayer thin-film assemblies with improved gas barrier." *Langmuir,* **21** 5919–5927 (2015)

47. Kim, H, Miura, Y, Macosko, CW, "Graphene/polyurethane nanocomposites for improved gas barrier and electrical conductivity." *Chem. Mater.,* **22** 3441–3450 (2010)

48. Chen, J, Yao, B, Li, C, Shi, GQ, "An improved Hummers method for eco-friendly synthesis of graphene oxide." *Carbon,* **64** 225–229 (2013)

49. Singhbabu, YN, Sivakumar, B, Singh, JK, Bapari, H, Pramanick, AK, Sahu, RK, "Efficient anti-corrosive coating of colled-rolled steel in a seawater environment using an oil-based graphene oxide ink." *Nanoscale,* **7** 8035–8047 (2015)

50. Mohammadi, S, Taromi, FA, Shariatpanahi, H, Neshati, J, Hemmati, M, "Electrochemical and anticorrosion behavior of functionalized graphite nanoplatelets epoxy coating." *J. Ind. Eng. Chem.,* **20** 4124–4139 (2014)

51. Yu, YH, Lin, YY, Lin, CH, Chan, CC, Huang, YC, "High-performance polystyrene/graphene-based nanocomposites with excellent anti-corrosion properties." *Polym. Chem.,* **5** 535–550 (2014)

52. Weng, CJ, Chang, CH, Peng, CW, Chen, SW, Yeh, JM, Hsu, CL, "Advanced anticorrosive coatings prepared from the mimicked *Xanthosoma sagittifolium*-leaf-like electroactive epoxy with synergistic effects of superhydrophobicity and redox catalytic capability." *Chem. Mater.,* **23** 2075–2083 (2011)

53. Liu, JG, Gong, GP, Yan, CW, "EIS study of corrosion behaviour of organic coating/dacromet composite systems." *Electrochim. Acta,* **50** 3320–3332 (2005)

54. Shreepathi, S, Naik, SM, Vattipalli, MR, "Water transportation through organic coatings: Correlation between electrochemical impedance measurements, gravimetry and water vapor permeability." *J. Coat. Technol. Res.,* **9** 411–422 (2012)

55. Behzadnasab, M, Mirabedini, SM, Kabiri, K, Jamali, S, "Corrosion performance of epoxy coatings containing silane treated ZrO_2 nanoparticles on mild steel in 3.5% NaCl solution." *Corros. Sci.,* **53** 89–98 (2011)

56. Zhu, CF, Xie, R, Xue, JH, Song, LL, "Studies of the impedance models and water transport behaviors of cathodically polarized coating." *Electrochim. Acta,* **56** 5828–5835 (2011)

57. Zhu, K, Li, XR, Wang, HH, Li, JY, Fei, GQ, "Electrochemical and anti-corrosion behaviors of water dispersible graphene/acrylic modified alkyd resin latex composites coated carbon steel." *J. Appl. Polym. Sci.,* **134** 1–12 (2017)

58. Ji, WG, Hu, JM, Liu, L, Zhang, JQ, Cao, CN, "Water uptake of epoxy coatings modified with γ-APS silane monomer." *Prog. Org. Coat.,* **57** 439–443 (2006)

59. Ramezanzadeh, B, Ahmadi, A, Mahdavian, M, "Enhancement of the corrosion protection performance and cathodic delamination resistance of epoxy coating through treatment of steel substrate by a novel nanometric sol-gel based silane composite film filled with functionalized graphene oxide nanosheets." *Corros. Sci.,* **109** 182–205 (2016)

60. Sathiyanarayanan, S, Azim, SS, Venkatachari, G, "A new corrosion protection coating with polyaniline-TiO_2 composite for steel." *Electrochim. Acta,* **52** 2068–2074 (2007)

61. Hsu, CH, Mansfeld, F, "Concerning the conversion of the constant phase element parameter Y_0 into a capacitance." *Corrosion,* **57** 747–748 (2001)

62. Dang, DN, Peraudeau, B, Cohendoz, S, Mallarino, S, Feaugas, X, Touzain, S, "Effect of mechanical stresses on epoxy coating ageing approached by electrochemical impedance spectroscopy measurements." *Electrochim. Acta,* **124** 80–89 (2014)

63. Bellucci, F, Nicodemo, L, "Water transport in organic coatings." *Corros. Sci.,* **49** 235–247 (1993)

64. Jiang, MY, Wu, LK, Hu, JM, Zhang, JQ, "Silane-incorporated epoxy coatings on aluminum alloy (AA2024). Part 1: Improved corrosion performance." *Corros. Sci.,* **92** 118–126 (2015)

65. Pahnke, J, Rühe, J, "Attachment of polymer films to aluminium surfaces by photochemically active monolayers of phosphonic acids." *Macromol. Rapid Commun.,* **25** 1396–1401 (2004)

66. Zhao, ZH, Guo, L, Feng, L, Lu, H, Xu, Y, Wang, JN, Xiang, B, Zou, XF, "Polydopamine functionalized graphene oxide nanocomposites reinforced the corrosion protection and adhesion properties of waterborne polyurethane coatings." *Eur. Polym. J.,* **120** 109249 (2019)

67. Bahlakeh, G, "A detailed molecular dynamics simulation and experimental investigation on the interfacial bonding

mechanism of an epoxy adhesive on carbon steel sheets decorated with a novel Cerium−Lanthanum nanofilm.'' *ACS Appl. Mater. Interfaces,* **9** 17536–17551 (2017)

68. Ramezanzadeh, B, Kardar, P, Bahlakeh, G, Hayatgheib, Y, Mahdavian, M, ''Fabrication of a highly tunable graphene oxide composite through layer-by-layer assembly of highly crystalline polyaniline nanofibers and green corrosion inhibitors: Complementary experimental and first-principles quantum-mechanics modeling approaches.'' *J. Phys. Chem. C,* **121** 20433–20450 (2017)

69. Bahlakeh, G, Ghaffari, M, Reza Saeb, M, Ramezanzadeh, B, De Proft, F, Terryn, H, ''A close-up of the effect of iron oxide type on the interfacial interaction between epoxy and carbon steel: Combined molecular dynamics simulations and quantum mechanics.'' *J. Phys. Chem. C,* **120** 11014–11026 (2016)

70. Ramezanzadeha, B, Bahlakehb, G, Mohamadzadeh Moghadamc, MH, Miraftaba, R, ''Impact of size-controlled p-phenylenediamine (PPDA)-functionalized graphene oxide nanosheets on the GO-PPDA/epoxy anti-corrosion, interfacial interactions and mechanical properties enhancement: Experimental and quantum mechanics investigations.'' *Chem. Eng. J.,* **335** 737–755 (2018)